

## APPLIED SCIENCES AND ENGINEERING

# One-component order parameter in URu<sub>2</sub>Si<sub>2</sub> uncovered by resonant ultrasound spectroscopy and machine learning

Sayak Ghosh<sup>1\*</sup>, Michael Matty<sup>1\*</sup>, Ryan Baumbach<sup>2</sup>, Eric D. Bauer<sup>3</sup>, K. A. Modic<sup>4</sup>, Arkady Shekhter<sup>2</sup>, J. A. Mydosh<sup>5</sup>, Eun-Ah Kim<sup>1</sup>, B. J. Ramshaw<sup>1†</sup>

The unusual correlated state that emerges in URu<sub>2</sub>Si<sub>2</sub> below  $T_{HO} = 17.5$  K is known as “hidden order” because even basic characteristics of the order parameter, such as its dimensionality (whether it has one component or two), are “hidden.” We use resonant ultrasound spectroscopy to measure the symmetry-resolved elastic anomalies across  $T_{HO}$ . We observe no anomalies in the shear elastic moduli, providing strong thermodynamic evidence for a one-component order parameter. We develop a machine learning framework that reaches this conclusion directly from the raw data, even in a crystal that is too small for traditional resonant ultrasound. Our result rules out a broad class of theories of hidden order based on two-component order parameters, and constrains the nature of the fluctuations from which unconventional superconductivity emerges at lower temperature. Our machine learning framework is a powerful new tool for classifying the ubiquitous competing orders in correlated electron systems.

## INTRODUCTION

Phase transitions mark the boundary between different states of matter, such as liquid to solid, or paramagnet to ferromagnet. At the phase transition, the system lowers its symmetry: Translationally invariant liquids become crystalline solids; paramagnetic spins align to break time reversal and rotation symmetry in a magnet. The conventional description of a second-order phase transition—Landau theory—requires knowledge of which symmetries are broken in the low-temperature phase to construct an order parameter (OP). Several possibilities have been put forth for the symmetry of the OP in the hidden order (HO) state of URu<sub>2</sub>Si<sub>2</sub> (Table 1), but most of these rely on specific microscopic mechanisms that are difficult to verify experimentally (1, 2).

The purpose of this paper was to use resonant ultrasound spectroscopy (RUS) to place strict thermodynamic constraints—independent of microscopic mechanism—on the OP symmetry in URu<sub>2</sub>Si<sub>2</sub>. While RUS is a powerful technique—capable of constraining or identifying the symmetries broken at a phase transition (3)—it has one substantial drawback: A single missing resonance renders an entire spectrum unusable. This is because traditional RUS data analysis relies on solving the elastic wave equation and mapping the computed resonances one to one with measured resonances—a single missing resonance invalidates this mapping. Here, we develop a new machine learning-based approach. We take advantage of the fact that neural networks can be trained to recognize features in complex datasets and classify the state of matter that produces such data (4–9). We validate this approach by analyzing an RUS dataset that we are confident can also be analyzed using traditional methods (data from a large single-crystal URu<sub>2</sub>Si<sub>2</sub> with a well-defined geometry). We then analyze data from a higher-quality URu<sub>2</sub>Si<sub>2</sub> sample that has an ill-defined geometry—a task that is impossible for the traditional analysis method but which is easily performed by our neural network.

While the broken symmetries of HO are unknown, most theories assume some form of “multipolar order,” whereby localized 5f electrons on the uranium site occupy orbitals that order below  $T_{HO} = 17.5$  K. However, direct experimental evidence for localized 5f electrons—such as crystalline electric field level splitting—does not exist (1), leaving room for theories of HO based on itinerant 5f electrons. Many possible OPs remain in contention, but, whether itinerant or localized, all theories of HO can be classified on the basis of the dimensionality of their point group representation: one component (10–19) or two component (20–26) [see Table 1 and (27)]. Theories of two-component OPs are motivated largely by the experiments of Okazaki *et al.* (28) and Tonegawa *et al.* (29), which detect a small  $C_4$  symmetry breaking at  $T_{HO}$ . More recent x-ray experiments have cast doubt on these results (30), leaving even the dimensionality of the OP in URu<sub>2</sub>Si<sub>2</sub> an open question.

Determining OP dimensionality is more than an exercise in accounting: The two-component nature of loop currents allows for dynamics that have been suggested to explain the pseudogap in high- $T_c$  cuprates (31), and the proposed two-component  $p_x + ip_y$  superconducting state of Sr<sub>2</sub>RuO<sub>4</sub> has a unique topological structure that can support Majorana fermions (32, 33). Establishing the dimensionality of the HO state not only allows us to rigorously exclude a large number of possible OPs but also provides a starting point for understanding the unusual superconductivity that emerges at lower temperature in URu<sub>2</sub>Si<sub>2</sub>.

## RESULTS

### RUS of URu<sub>2</sub>Si<sub>2</sub>

RUS measures the mechanical resonance frequencies of a single-crystal specimen—analogue to the harmonics of a guitar string but in three dimensions (see Fig. 1A). A subset of this spectrum for a 3 mm by 2.8 mm by 2.6 mm crystal of URu<sub>2</sub>Si<sub>2</sub> (sample S1) is shown in Fig. 1B, with each peak occurring at a unique eigenfrequency of the elastic wave equation (see the Supplementary Materials). Encoded within these resonances is information about the sample’s dimensions and density, which are known, and the six elastic moduli, which are unknown. As electrons and phonons are coupled strongly in metals, the temperature dependence of the elastic moduli reveals

Copyright © 2020  
The Authors, some  
rights reserved;  
exclusive licensee  
American Association  
for the Advancement  
of Science. No claim to  
original U.S. Government  
Works. Distributed  
under a Creative  
Commons Attribution  
NonCommercial  
License 4.0 (CC BY-NC).

<sup>1</sup>Laboratory of Atomic and Solid State Physics, Cornell University, Ithaca, NY 14853, USA. <sup>2</sup>National High Magnetic Field Laboratory, Florida State University, Tallahassee, FL 32310, USA. <sup>3</sup>Los Alamos National Laboratory, Los Alamos, NM 87545, USA. <sup>4</sup>Max Planck Institute for Chemical Physics of Solids, Dresden 01187, Germany. <sup>5</sup>Kamerlingh Onnes Laboratory and Institute Lorentz, Leiden University, 2300RA Leiden, Netherlands.

\*These authors contributed equally to this work.

†Corresponding author. Email: bradramshaw@cornell.edu

**Table 1. Proposed OPs of the HO state in URu<sub>2</sub>Si<sub>2</sub>, classified by their dimensionality and their point group representation.** Note that designations such as “hexadecapole” order are only applicable in free space—crystalline electric fields break these large multipoles into the representations listed in this table.

| Dimensionality | Symmetry    | Reference  |
|----------------|-------------|--|
| One-component  | $A_{1g}$    | Harrison and Jaime (53)  |
|                | $A_{1u}$    | Kambe <i>et al.</i> (19)   |
|                | $A_{2g}$    | Haule and Kotliar (14), Kusunose and Harima (15), and Kung <i>et al.</i> (17)                            |
|                | $A_{2u}$    | Cricchio <i>et al.</i> (16)  |
|                | $B_{1g}$    | Ohkawa and Shimizu (11) and Santini and Amoretti (12)  |
|                | $B_{1u}$    | Kiss and Fazekas (13)  |
|                | $B_{2g}$    | Ohkawa and Shimizu (11), Santini and Amoretti (12), and Harima <i>et al.</i> (10)                        |
|                | $B_{2u}$    | Kiss and Fazekas (13)  |
| Two-component  | $E_g$       | Thalmeier and Takimoto (20), Tonegawa <i>et al.</i> (23), Rau and Kee (22), and Riggs <i>et al.</i> (26) |
|                | $E_u$       | Hoshino <i>et al.</i> (21), Ikeda <i>et al.</i> (25), and Riggs <i>et al.</i> (26)                       |
|                | $E_{3/2,g}$ | Chandra <i>et al.</i> (54)   |
|                |             |  |

fluctuations and instabilities in the electronic subsystem. In particular, elastic moduli are sensitive to symmetry breaking at electronic phase transitions (3, 34). The difficulty lies in converting the temperature dependence of the resonance spectrum into the temperature dependence of the elastic moduli. The traditional analysis involves solving the three-dimensional (3D) elastic wave equation and adjusting the elastic moduli to match the experimental resonance spectrum. However, if even a single resonance is missing from the spectrum (e.g., due to weak coupling of a particular mode to the transducers), then this analysis scheme breaks down [see Ramshaw *et al.* (3) for further discussion of this problem].

Figure 1C shows the temperature dependence of seven representative elastic resonances through  $T_{HO}$  (29 resonances were measured in total). Note that while some resonances show a step-like discontinuity or “jump” at  $T_{HO}$ , others do not. This jump is present in the elastic moduli for all second-order phase transitions (3, 34, 35) but has never before been observed in URu<sub>2</sub>Si<sub>2</sub> due to insufficient experimental resolution (36–40). Traditional RUS produces spectra at each temperature, such as the one shown in Fig. 1B, by sweeping the entire frequency range using a lock-in amplifier. The resonance frequencies are then extracted by fitting Lorentzians to each peak (34). We have developed a new approach whereby the entire spectrum is swept only once—to identify the resonances—and then, each resonance is tracked as a function of temperature with high precision using a phase-locked loop. This increases

the density of data points per unit temperature by roughly a factor of 1000 and increases the signal-to-noise by a factor of 30 (see Materials and Methods).

The complex strain fields produced at each resonance frequency (Fig. 1A) can be broken down locally into irreducible representations of strain ( $\epsilon_k$ ). Each irreducible strain then couples to an OP  $\eta$  of a particular symmetry in a straightforward manner (35). In this way, analysis of the temperature dependence of the resonance frequencies can identify or constrain the OP symmetry. In a tetragonal crystal, such as URu<sub>2</sub>Si<sub>2</sub>, elastic strain breaks into five irreducible representations (Fig. 2): two compressive strains transforming as the identity  $A_{1g}$  representation, and three shear strains transforming as the  $B_{1g}$ ,  $B_{2g}$ , and  $E_g$  representations. Allowed terms in the free energy  $\mathcal{F}$  are products of strains and OPs that transform as the  $A_{1g}$  representation. As HO is thought to break at least translational symmetry, the lowest-order terms allowed by both one-component and two-component OPs are linear in the  $A_{1g}$  strains and quadratic in OP:  $\mathcal{F} = \epsilon_{A_{1g}} \cdot \eta^2$  [see (41)]. Quadratic-in-order-parameter, linear-in-strain coupling produces a discontinuity in the associated elastic modulus at the phase transition: This jump is related to discontinuities in the specific heat and other thermodynamic quantities through Ehrenfest relations (34, 42). For OPs with one-component representations (any of the  $A_i$  or  $B_i$  representations of  $D_{4h}$ ), only the elastic moduli corresponding to  $A_{1g}$  compressional strains couple in this manner. In contrast, shear strains couple as  $\mathcal{F} = \epsilon_k^2 \cdot \eta^2$  and show at most a change in slope at  $T_{HO}$  (3). Thus  $c_{33}$ ,  $c_{23}$ , and  $(c_{11} + c_{12})/2$  may exhibit jumps at phase transitions corresponding to one-component OPs, while  $(c_{11} - c_{12})/2$ ,  $c_{66}$ , and  $c_{44}$  cannot.

Two-component OPs (of the  $E_i$  representations), on the other hand, have bilinear forms that can couple with two of the shear strains to first order. A two-component OP,  $\vec{\eta} = \{\eta_x, \eta_y\}$ , has the bilinears  $\eta_x^2 + \eta_y^2$ ,  $\eta_x^2 - \eta_y^2$ , and  $\eta_x \eta_y$  of the  $A_{1g}$ ,  $B_{1g}$ , and  $B_{2g}$  representations, respectively. In addition to the standard  $\epsilon_{A_{1g}} \cdot \eta_x^2 + \eta_y^2$  terms, the free energy now contains the terms  $\epsilon_{B_{1g}} \cdot (\eta_x^2 - \eta_y^2)$  and  $\epsilon_{B_{2g}} \cdot \eta_x \eta_y$ . A second-order phase transition characterized by a two-component OP therefore exhibits discontinuities in the  $B_{1g}$  and  $B_{2g}$  shear elastic moduli [ $(c_{11} - c_{12})/2$  and  $c_{66}$ , respectively], in addition to jumps in the compressional  $A_{1g}$  moduli (see the Supplementary Materials for a discussion of the  $E_{3/2,g}$  representation, pertaining to “hastatic” order).

We first perform a traditional RUS analysis, extracting the temperature dependence of the six elastic moduli (Fig. 2, B and C) from 29 measured resonances by solving the elastic wave equation and fitting the spectrum using a genetic algorithm [see the Supplementary Materials of Ramshaw *et al.* (3) for details]. The evolution of the elastic moduli across  $T_{HO}$  shows jumps in two of the  $A_{1g}$  elastic moduli, whereas the  $B_{1g}$  and  $B_{2g}$  shear moduli show only a break in slope at  $T_{HO}$  to within our experimental uncertainty (Fig. 2D). Jumps in the shear moduli would be expected for any OP of the two-component  $E_i$  representations (20–26)—the fact that we do not resolve any shear jumps constrains the OP of the HO phase to belong to a one-component representation of  $D_{4h}$ . The fact that we do not resolve a jump in  $c_{33}$  is consistent with the magnitudes of the jumps in  $(c_{11} + c_{12})/2$  and  $c_{23}$  (see the Supplementary Materials for details).

In principle, this traditional analysis is sufficient to determine the order-parameter dimensionality in URu<sub>2</sub>Si<sub>2</sub>. The process of solving for the elastic moduli, however, incorporates systematic errors arising from sample alignment, parallelism, dimensional uncertainty, and thermal contraction. Even more detrimental is the possibility that

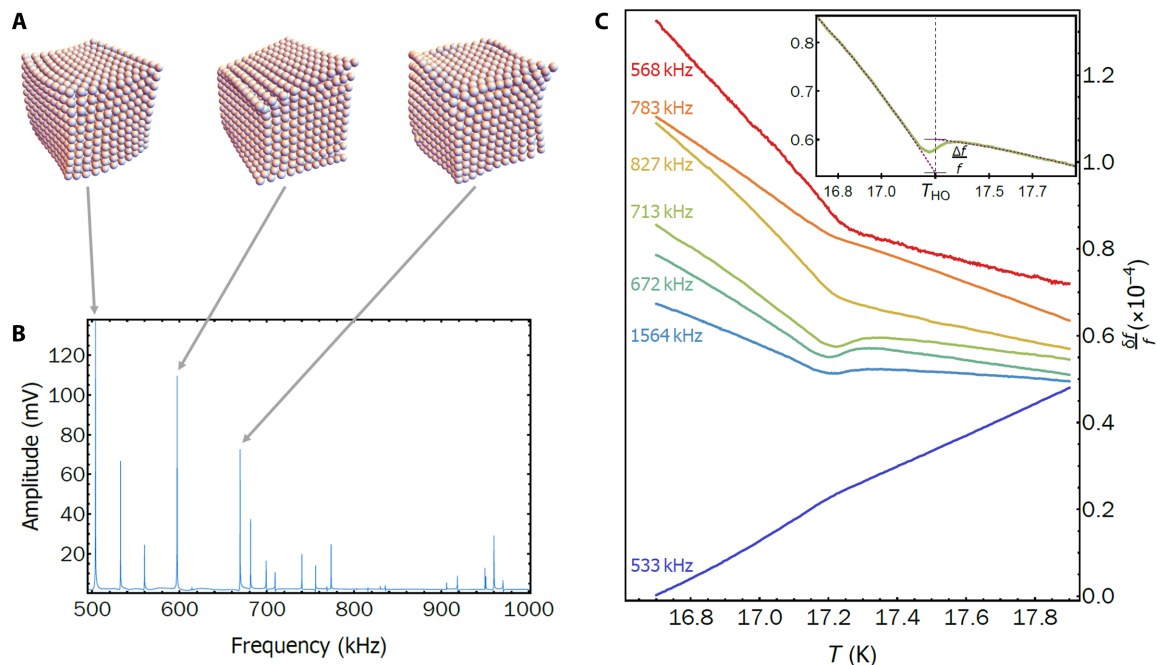


**Fig. 1. RUS across  $T_{HO}$  in  $URu_2Si_2$ .** (A) Schematic resonance eigenmodes obtained as a solution to the 3D elastic wave equation. Each mode contains a unique proportion of the five irreducible strains (see Fig. 2A). (B) Room temperature ultrasonic spectrum of sample S1, shown between 500 kHz and 1 MHz. (C) Temperature evolution of seven characteristic resonances, out of 29 total measured resonances, near the HO transition—plots are shifted vertically for clarity. Three resonances (672, 713, and 1564 kHz) show jumps at  $T_{HO}$  (inset illustrates what is meant by the jump), while the others do not, signifying contributions from different symmetry channels.

the measured spectrum is missing a resonance, rendering the entire analysis incorrect. While we are confident in our analysis for the particularly large and well-oriented sample S1, large samples of  $URu_2Si_2$  are known to be of slightly lower quality (43). Smaller, higher-quality crystals of  $URu_2Si_2$  do not lend themselves well to RUS studies, being hard to align and polish to high precision. Smaller samples also produce weaker RUS signals, making it easier to miss a resonance. We have therefore developed a new method for extracting symmetry information directly from the resonance spectrum, without needing to first extract the elastic moduli themselves, even if the spectrum is incomplete. This method takes advantage of the power of machine learning algorithms to recognize patterns in complex datasets.

### Machine learning for RUS

Artificial neural networks (ANNs) are popular machine learning tools due to their ability to classify objects in highly nonlinear ways. In particular, ANNs can approximate smooth functions arbitrarily well (44). Here, we train an ANN to learn a function that maps the jumps in ultrasonic resonances at a phase transition to one of two classes, corresponding to either a one-component or two-component OP. One-component OPs induce jumps only in compressional elastic moduli, whereas two-component OPs also induce jumps in two of the shear moduli. Phase transitions with two-component OPs should therefore show jumps in more ultrasonic resonances at a phase transition than phase transitions with one-component OPs. Our intent is that this difference in the distribution of jumps can be learned by an ANN to discriminate between one-component and two-component OPs.

An ANN must be trained with simulated data that encompass a broad range of possible experimental scenarios. In our case, we simulate RUS spectra given assumptions about the sample and the OP dimensionality. Starting with a set of parameters randomly generated within bounds that we specify—these include the sample geometry, density, and the six elastic moduli—we solve the elastic wave equation to produce the first  $N$  resonance frequencies that would be measured in an RUS experiment. Then, using a second set of assumptions—whether the OP has one component or two, whether our simulated experiment has  $k$  missing resonances, and the relative sizes of the elastic constant jumps produced at  $T_{HO}$ —we calculate the jumps at  $T_{HO}$  for the first  $n$  resonances (see Fig. 3). By varying the input assumptions, we produce a large number of training datasets that are intended to encompass the (unknown) experimental parameters.

While the sample geometry, density, and moduli are well determined for sample S1 and only varied by a few tens of percent, the dimensionality of the OP, the number of missing resonances, and the sizes of the jumps in each symmetry channel are taken to be completely unknown. We vary these latter parameters across a broad range of physically possible values (see Fig. 3 and the Supplementary Materials for further details). To prepare the simulated data for interpretation by our ANN, we take the first  $n$  jumps, sort the jumps by size, normalize the jumps to lie between zero and one, and label the datasets by the dimensionality of the OP that was used to create them—either one component or two.

This normalized and sorted list of numbers  $\{\Delta f_i/f_i\}$  is used as input to an ANN. Our ANN architecture is a fully connected, feedforward neural network with a single hidden layer containing 20 neurons (see Fig. 3). Each neuron  $j$  processes the inputs  $\{\Delta f_i/f_i\}$  according to the weight matrix

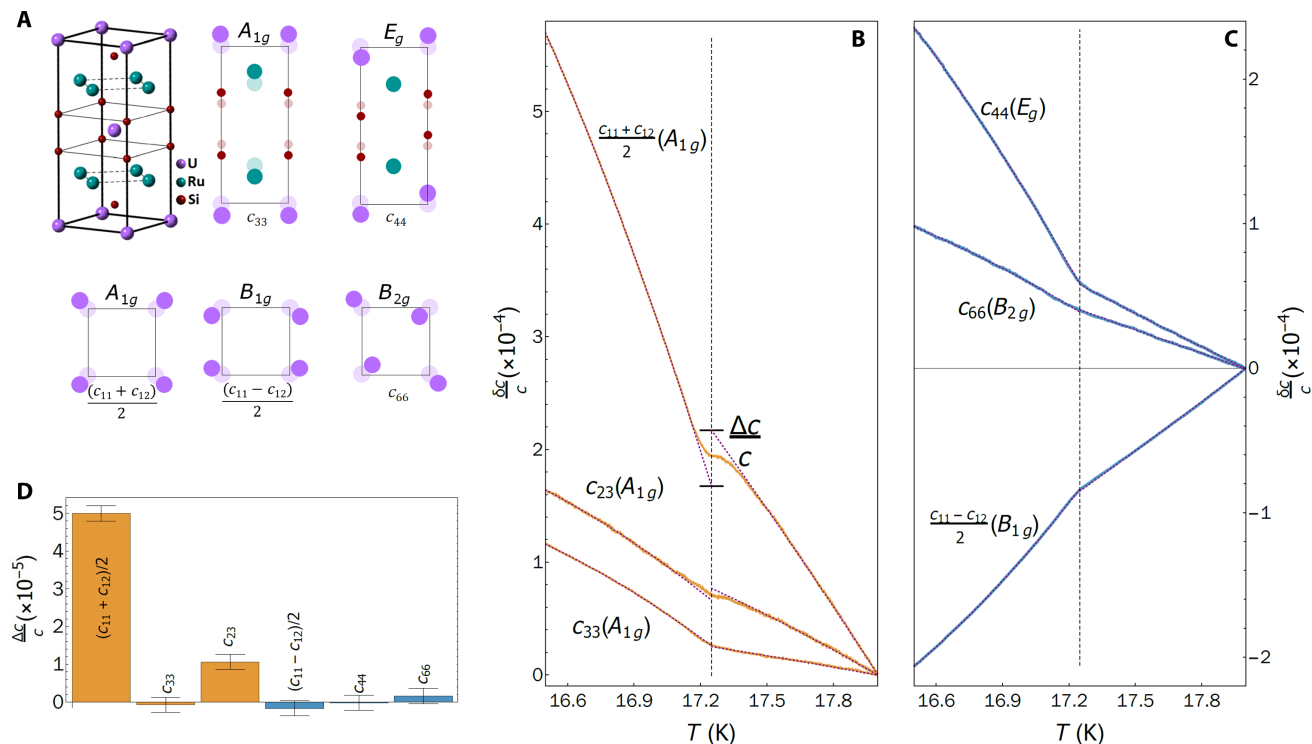


**Fig. 2. Traditional extraction of symmetry information from elastic moduli.** (A) The tetragonal crystal structure of URu<sub>2</sub>Si<sub>2</sub> and its five irreducible representations of strain, along with the associated moduli. Each resonance shown in Fig. 1A can be decomposed into this basis set of strains, modulated in phase at long wavelengths throughout the crystal.  $c_{23}$  characterizes the direct coupling between the two A<sub>1g</sub> strains. (B) Compressive (A<sub>1g</sub> shown in orange) and (C) shear (B<sub>1g</sub>, B<sub>2g</sub>, and E<sub>g</sub> shown in blue) elastic moduli, with dashed guides to the eye showing the temperature dependence extrapolated from below and above T<sub>HO</sub>. The absolute values (in gigapascals) of the moduli at ~20 K were determined to be  $(c_{11} + c_{12})/2 = 218.0$ ,  $c_{33} = 307.4$ ,  $c_{23} = 112.8$ ,  $(c_{11} - c_{12})/2 = 65.2$ ,  $c_{66} = 140.6$ , and  $c_{44} = 101.8$ . (D) The magnitude of the jumps at T<sub>HO</sub> with their experimental uncertainties. A large jump occurs in  $(c_{11} + c_{12})/2$  at T<sub>HO</sub>, along with a small jump in  $c_{23}$ . The shear moduli, on the other hand, show only a change in slope at T<sub>HO</sub>—this constrains the OP of the HO state to transform as a one-component representation.

$w_{ji}$  and the bias vector  $b_j$  specific to that neuron as  $\sigma(w_{ji}x_i + b_j)$ , where the rectified linear activation function is given by  $\sigma(y) \equiv \max(y, 0)$ . The sum of the neural outputs is normalized via a softmax layer.

We train the ANN using 10,000 sets of simulated RUS data for the case of a one-component OP, with varied elastic constants, sample geometries, jump magnitudes, and missing resonances, and another 10,000 sets for the case of a two-component OP. We use cross-entropy as the cost function for stochastic gradient descent. We train 10 different neural networks in this way to an accuracy of ~90% and then fix each individual network's weights and biases. Once the networks are trained, we ask each ANN for its judgment on the OP dimensionality associated with an experimentally determined set of 29 jumps and average the responses from each neural network. The sizes of the jumps depend on how T<sub>HO</sub> is assigned—assigning T<sub>HO</sub> artificially far from the actual phase transition will produce large jumps in all resonances. We therefore repeat our ANN determination using a range of T<sub>HO</sub> around the phase transition and plot the outcome as a function of T<sub>HO</sub>.

Figure 4A shows the results of our ANN analysis for sample S1—the same sample discussed above using the traditional analysis. To visually compare the training and experimental data in a transparent fashion, we plot the list of sorted and normalized jumps against their indices in the list. The average of the one-component training data is shown in red; the average of the two-component training data is shown in blue; the experimental jumps are shown in gray.

It is clear that the experimental data resemble the one-component training data much more closely. This resemblance is quantified in the inset, showing the ANN confidence that the experimental data belong to the one-component class for varying assignments of T<sub>HO</sub>. We find that the confidence of a one-component OP is maximized in the region of assigned T<sub>HO</sub> that corresponds to the experimental value of T<sub>HO</sub>.

Thus far, we have shown that both methods—the traditional method of extracting the elastic moduli using the elastic wave equation and our new method of examining the resonance spectrum directly using a trained ANN—agree that the HO parameter of URu<sub>2</sub>Si<sub>2</sub> is one component. We can now use the neural network to analyze a smaller, irregular-shaped but higher-quality [higher T<sub>HO</sub> (43)] sample that cannot be analyzed using the traditional method due to its complicated geometry. Figure 4B shows the result of the ANN analysis performed on a resonance spectrum of sample S2. The sorted and normalized spectrum looks very similar to that of sample S1, and the averaged ANN outcome gives 90% confidence that the OP is one component. Despite the fact that sample S2 has a geometry such that the elastic moduli cannot be extracted, its resonance spectrum still contains information about the OP dimensionality, and our ANN identifies this successfully.

## DISCUSSION

Our two analyses of ultrasonic resonances across T<sub>HO</sub> in URu<sub>2</sub>Si<sub>2</sub> strongly support one-component OPs, such as electric-hexadecapolar

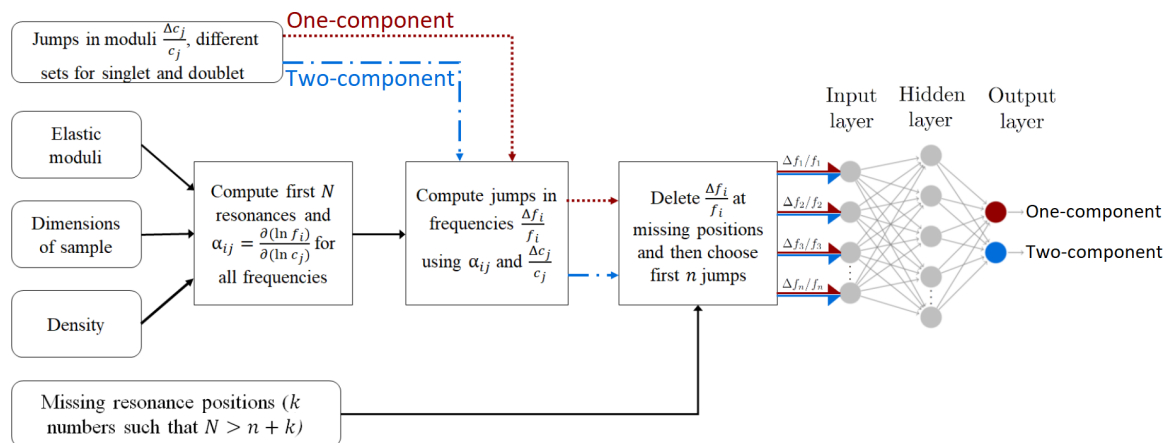


**Fig. 3. Schematic of the algorithm used to generate the training data.** Values for elastic moduli and dimensions are chosen randomly from a range that bounds our experimental uncertainties. One-component OPs give jumps only in  $A_{1g}$  moduli, whereas two-component OPs also give jumps in  $B_{1g}$  and  $B_{2g}$  moduli. Separate output files are generated corresponding to one-component and two-component OPs, each containing  $n$  jumps, where  $n$  is the number of frequencies whose temperature evolution could be experimentally measured. We use scaled RUS frequency shifts  $\Delta f_i/f_i$  as input to the ANN. The neurons in the hidden layer have weights  $w_{ij}$  and biases  $b_i$ . Each output neuron corresponds to one of the two OP dimensionalities under consideration, i.e., one-component and two-component. The output value of each neuron is the network's judgment on the likelihood of that OP dimensionality.

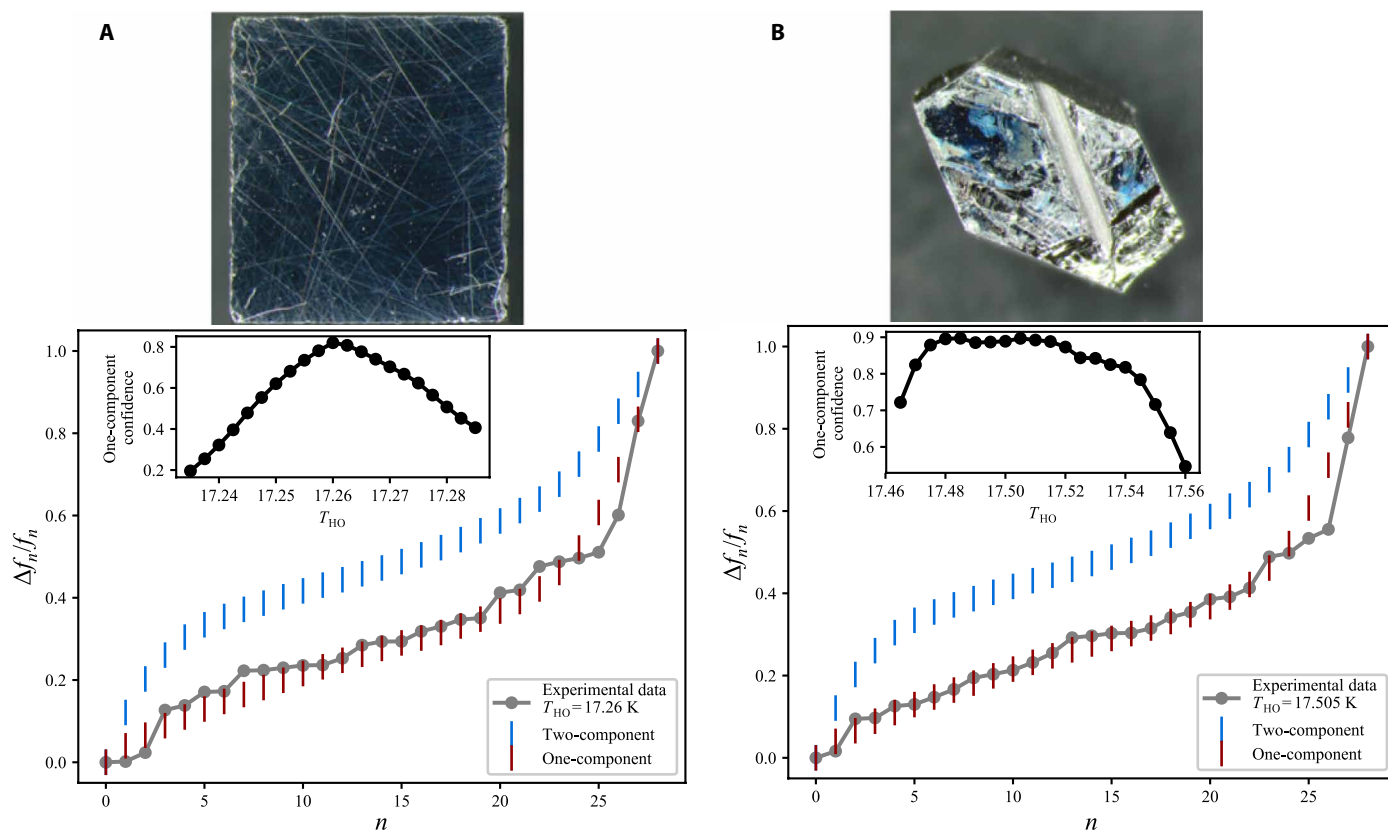


**Fig. 4. Results of the ANN analysis for two samples of  $URu_2Si_2$ .** Upper blue curves show the averaged, sorted, simulated frequency shift (jump) data plotted against its index in the sorted list for a two-component OP for (A) sample S1 and (B) sample S2. The data are normalized to range from 0 to 1. Lower, red curves shows the same for a one-component OP. Gray dots show experimental data for critical temperature assignment (A)  $T_{HO} = 17.26$  K and (B)  $T_{HO} = 17.505$  K, which visually aligns more closely with the average one-component simulated data than the two-component simulations. Insets: Percentage confidence of the one-component output neuron for various assignments of  $T_{HO}$  averaged over 10 trained networks. A maximum confidence of (A) 83.2% occurs for  $T_{HO} = 17.26$  K, and (B) 89.7% for  $T_{HO} = 17.505$  K. Sample S2 has a higher value of  $T_{HO}$  due to its lower impurity concentration, as verified independently by the resistivity. Photo credit: Sayak Ghosh, Cornell University.

order (14), the chiral density wave observed by Raman spectroscopy (17, 18, 45), and are consistent with the lack of  $C_4$  symmetry breaking observed in recent x-ray scattering experiments (30). Our analysis rules against two-component OPs, such as rank-5 superspin (19, 22) and spin nematic order (24). The power of our result lies in its independence from the microscopic origin of the OP: Group theoretical arguments alone are sufficient to rule out large numbers of possible OPs. It could be argued that the coupling constants governing the jumps in the shear moduli are sufficiently small such that the jumps are below our experimental resolution. Previous experiments, however, have shown these coupling constants to be of the same order of magnitude in other materials with multicomponent OPs (35, 46, 47). It has also been demonstrated that the size of the jump in heat capacity at  $T_{HO}$  is largely insensitive to residual resistivity ratio (RRR) (43, 48, 49). It is therefore hard to imagine that higher RRR samples would yield jumps in the shear moduli.

The use of ANNs to analyze RUS data represents an exciting opportunity to reexamine ultrasound experiments that were previously unable to identify OP symmetry. For example, irregular sample geometry prevented identification of the OP symmetry in the high- $T_c$  superconductor  $YBa_2Cu_3O_{6.98}$  (34). Reanalysis of this spectrum using our ANN could reveal whether the OP of the pseudogap is associated with  $E_u$ -symmetry orbital loop currents. The proposed two-component  $p_x + ip_y$  superconducting state of  $Sr_2RuO_4$  and other potential spin-triplet superconductors could also be identified in this fashion, where traditional pulse-echo ultrasound measurements have been confounded by systematic uncertainty (50).

Beyond RUS, there are many other data analysis problems in experimental physics that stand to be improved using an approach similar to the one presented here (51). In particular, any technique where simulation of a dataset is straightforward but where fitting is difficult should be amenable to a framework of the type used here. The most immediately obvious technique where our algorithm could be applied is nuclear magnetic resonance (NMR) spectroscopy. NMR produces spectra in a similar frequency range to RUS but which originate in the spin-resonances of nuclear magnetic moments. Modern broadband NMR can produce complex temperature-dependent spectra, containing resonances from multiple elements situated at different sites within the unit cell. Given a particular magnetic order, it is relatively straightforward to calculate the NMR spectrum—i.e., to produce training data. The inverse problem, however, is more challenging: recovering a temperature-dependent magnetic structure from an NMR dataset. In a way similar to RUS, missing resonances and resonances mistakenly attributed to different elements can render an analysis entirely invalid. It should be relatively straightforward to adapt our framework for generating training data and our ANN to extract temperature (or magnetic field)-dependent magnetic structures from NMR spectra.

## MATERIALS AND METHODS

Sample S1 was grown by the Czochralski method. A single crystal oriented along the crystallographic axes was polished to dimensions 3.0 mm by 2.8 mm by 2.6 mm, with 2.6 mm along the tetragonal long axis. Sample S2 was grown by the Czochralski method and then processed by solid-state electrorefinement. Typical RRR values for  $ab$ -plane flakes of  $URu_2Si_2$  taken from the larger piece range from 100 to 500. The RRR values measured on larger pieces (Fig. 4) are between 10 and 20. For a comparison of different growth methods for  $URu_2Si_2$  see Gallagher *et al.* (49).

Resonant ultrasound experiments were performed in a custom-built setup consisting of two compressional-mode lithium niobate transducers, which were vibrationally isolated from the rest of the apparatus. The top transducer was mounted on a freely pivoting arm, ensuring weak coupling and linear response. The response voltage generated on the pickup transducer—maximum whenever the drive frequency coincides with a sample resonance—was measured with lock-in technique. The response signal was preamplified using a custom-made charge amplifier to compensate for signal degradation in coaxial cables (52). Oxford Instruments He<sup>4</sup> cryostat was used for providing temperature control.

## SUPPLEMENTARY MATERIALS

Supplementary material for this article is available at <http://advances.sciencemag.org/cgi/content/full/6/10/eaaz4074/DC1>

Phase-locked loop  
Training data for ANN  
Symmetry and coupling  
Lack of  $\epsilon_{33}$  jump  
Resolving the origin of jumps  
Compositions of resonances  
Resistance measurement  
Possible effects from parasitic antiferromagnetism  
Table S1. Calculated discontinuities ("jumps") in elastic moduli for one- and two-component OPs in a tetragonal system.  
Fig. S1. Resonant ultrasound using phase-locked loop.  
Fig. S2. Three representative resonance frequencies of  $URu_2Si_2$  and their attenuation through  $T_{HO}$ .  
Fig. S3. Elastic moduli of  $URu_2Si_2$  with the contribution above  $T_{HO}$  subtracted.  
Fig. S4. Fitting temperature evolution of resonances.  
Fig. S5. Resistance of sample S2 measured from 300 K down to 2 K.  
References (55–59)

## REFERENCES AND NOTES

1. J. A. Mydosh, P. M. Oppeneer, Colloquium: Hidden order, superconductivity, and magnetism: The unsolved case of  $URu_2Si_2$ . *Rev. Mod. Phys.* **83**, 1301 (2011).
2. J. Mydosh, P. Oppeneer, Hidden order behaviour in  $URu_2Si_2$  (A critical review of the status of hidden order in 2014). *Philos. Mag.* **94**, 3642–3662 (2014).
3. B. J. Ramshaw, A. Shekhter, R. D. McDonald, J. B. Betts, J. N. Mitchell, P. H. Tobash, C. H. Mielke, E. D. Bauer, A. Migliori, Avoided valence transition in a plutonium superconductor. *Proc. Natl. Acad. Sci. U.S.A.* **112**, 3285–3289 (2015).
4. J. Carrasquilla, R. G. Melko, Machine learning phases of matter. *Nat. Phys.* **13**, 431–434 (2017).
5. R. Ouyang, S. Curtarolo, E. Ahmetcik, M. Scheffler, L. M. Ghiringhelli, SISO: A compressed-sensing method for identifying the best low-dimensional descriptor in an immensity of offered candidates. *Phys. Rev. Mater.* **2**, 083802 (2018).
6. A. Bohrdt, C. S. Chiu, G. Ji, M. Xu, D. Greif, M. Greiner, E. Demler, F. Grusdt, M. Knap, Classifying snapshots of the doped Hubbard model with machine learning. *Nat. Phys.* **15**, 921–924 (2019).
7. B. S. Rem, N. Käming, M. Tarnowski, L. Asteria, N. Fläschner, C. Becker, K. Sengstock, C. Weitenberg, Identifying quantum phase transitions using artificial neural networks on experimental data. *Nat. Phys.* **15**, 917–920 (2019).
8. Y. Zhang, A. Mesaros, K. Fujita, S. D. Edkins, M. H. Hamidian, K. Ch'ng, H. Eisaki, S. Uchida, J. C. S. Davis, E. Khatami, E.-A. Kim, Machine learning in electronic-quantum-matter imaging experiments. *Nature* **570**, 484–490 (2019).
9. Y. Yamaji, T. Yoshida, A. Fujimori, M. Imada, Hidden self-energies as origin of cuprate superconductivity revealed by machine learning. arXiv:1903.08060 [cond-mat.str-el] (19 March 2019).
10. H. Harima, K. Miyake, J. Flouquet, Why the hidden order in  $URu_2Si_2$  is still hidden—one simple answer. *J. Phys. Soc. Japan* **79**, 033705 (2010).
11. F. J. Ohkawa, H. Shimizu, Quadrupole and dipole orders in  $URu_2Si_2$ . *J. Phys. Condens. Matter* **11**, L519 (1999).
12. P. Santini, G. Amoretti, Crystal field model of the magnetic properties of  $URu_2Si_2$ . *Phys. Rev. Lett.* **73**, 1027–1030 (1994).
13. A. Kiss, P. Fazekas, Group theory and octupolar order in  $URu_2Si_2$ . *Phys. Rev. B* **71**, 054415 (2005).
14. K. Haule, G. Kotliar, Arrested Kondo effect and hidden order in  $URu_2Si_2$ . *Nat. Phys.* **5**, 796–799 (2009).
15. H. Kusunose, H. Harima, On the hidden order in  $URu_2Si_2$ —Antiferro hexadecapole order and its consequences. *J. Phys. Soc. Japan* **80**, 084702 (2011).

16. F. Cricchio, F. Bultmark, O. Grånäs, L. Nordström, Itinerant magnetic multipole moments of rank five as the hidden order in URu<sub>2</sub>Si<sub>2</sub>. *Phys. Rev. Lett.* **103**, 107202 (2009).
17. H.-H. Kung, R. E. Baumbach, E. D. Bauer, V. K. Thorsmølle, W.-L. Zhang, K. Haule, J. A. Mydosh, G. Blumberg, Heavy fermions. Chirality density wave of the “hidden order” phase in URu<sub>2</sub>Si<sub>2</sub>. *Science* **347**, 1339–1342 (2015).
18. H.-H. Kung, S. Ran, N. Kanchanavatee, V. Krapišin, A. Lee, J. A. Mydosh, K. Haule, M. B. Maple, G. Blumberg, Analogy between the “hidden order” and the orbital antiferromagnetism in URu<sub>2-x</sub>Fe<sub>x</sub>Si<sub>2</sub>. *Phys. Rev. Lett.* **117**, 227601 (2016).
19. S. Kambe, Y. Tokunaga, H. Sakai, T. Hattori, N. Higa, T. D. Matsuda, Y. Haga, R. E. Walstedt, H. Harima, Odd-parity electronic multipolar ordering in URu<sub>2</sub>Si<sub>2</sub>: Conclusions from Si and Ru NMR measurements. *Phys. Rev. B* **97**, 235142 (2018).
20. P. Thalmeier, T. Takimoto, Signatures of hidden-order symmetry in torque oscillations, elastic constant anomalies, and field-induced moments in URu<sub>2</sub>Si<sub>2</sub>. *Phys. Rev. B* **83**, 165110 (2011).
21. S. Hoshino, J. Otsuki, Y. Kuramoto, Resolution of entropy  $\ln 2$  by ordering in two-channel kondo lattice. *J. Phys. Soc. Japan* **82**, 044707 (2013).
22. J. G. Rau, H.-Y. Kee, Hidden and antiferromagnetic order as a rank-5 superspin in URu<sub>2</sub>Si<sub>2</sub>. *Phys. Rev. B* **85**, 245112 (2012).
23. S. Tonegawa, K. Hashimoto, K. Ikeda, Y.-H. Lin, H. Shishido, Y. Haga, T. D. Matsuda, E. Yamamoto, Y. Onuki, H. Ikeda, Y. Matsuda, T. Shibauchi, Cyclotron resonance in the hidden-order phase of URu<sub>2</sub>Si<sub>2</sub>. *Phys. Rev. Lett.* **109**, 036401 (2012).
24. S. Fujimoto, Spin nematic state as a candidate of the hidden order phase of URu<sub>2</sub>Si<sub>2</sub>. *Phys. Rev. Lett.* **106**, 196407 (2011).
25. H. Ikeda, M.-T. Suzuki, R. Arita, T. Takimoto, T. Shibauchi, Y. Matsuda, Emergent rank-5 nematic order in URu<sub>2</sub>Si<sub>2</sub>. *Nat. Phys.* **8**, 528–533 (2012).
26. S. C. Riggs, M. C. Shapiro, A. V. Maharaj, S. Raghu, E. D. Bauer, R. E. Baumbach, P. Giraldo-Gallo, M. Wartenbe, I. R. Fisher, Evidence for a nematic component to the hidden-order parameter in URu<sub>2</sub>Si<sub>2</sub> from differential elastoresistance measurements. *Nat. Commun.* **6**, 6425 (2015).
27. It is also generally agreed that OP of the HO state orders at a finite wavevector of  $Q = (0, 0, 1/2)$ . Because our measurement occurs close to  $Q = 0$ , i.e., at long wavelength, we are only concerned with the point group symmetry of the OP and not with its modulation in space.
28. R. Okazaki, T. Shibauchi, H. J. Shi, Y. Haga, T. D. Matsuda, E. Yamamoto, Y. Onuki, H. Ikeda, Y. Matsuda, Rotational symmetry breaking in the hidden-order phase of URu<sub>2</sub>Si<sub>2</sub>. *Science* **331**, 439–442 (2011).
29. S. Tonegawa, S. Kasahara, T. Fukuda, K. Sugimoto, N. Yasuda, Y. Tsuruhara, D. Watanabe, Y. Mizukami, Y. Haga, T. D. Matsuda, E. Yamamoto, Y. Onuki, H. Ikeda, Y. Matsuda, T. Shibauchi, Direct observation of lattice symmetry breaking at the hidden-order transition in URu<sub>2</sub>Si<sub>2</sub>. *Nat. Commun.* **5**, 4188 (2014).
30. J. Choi, O. Ivashko, N. Dennler, D. Aoki, K. von Arx, S. Gerber, O. Gutowski, M. H. Fischer, J. Stremfper, M. v. Zimmermann, J. Chang, Pressure-induced rotational symmetry breaking in URu<sub>2</sub>Si<sub>2</sub>. *Phys. Rev. B* **98**, 241113 (2018).
31. V. Aji, A. Shekhter, C. M. Varma, Theory of the coupling of quantum-critical fluctuations to fermions and *d*-wave superconductivity in cuprates. *Phys. Rev. B* **81**, 064515 (2010).
32. T. Rice, M. Sigrist, Sr<sub>2</sub>RuO<sub>4</sub>: An electronic analogue of <sup>3</sup>He? *J. Phys. Condens. Matter* **7**, L643 (1995).
33. N. Read, D. Green, Paired states of fermions in two dimensions with breaking of parity and time-reversal symmetries and the fractional quantum Hall effect. *Phys. Rev. B* **61**, 10267 (2000).
34. A. Shekhter, B. J. Ramshaw, R. Liang, W. N. Hardy, D. A. Bonn, F. F. Balakirev, R. D. McDonald, J. B. Betts, S. C. Riggs, A. Migliori, Bounding the pseudogap with a line of phase transitions in YBa<sub>2</sub>Cu<sub>3</sub>O<sub>6+x</sub>. *Nature* **498**, 75–77 (2013).
35. B. Lüthi, T. J. Moran, Sound propagation near the structural phase transition in strontium titanate. *Phys. Rev. B* **2**, 1211 (1970).
36. T. Fukase, Y. Koike, T. Nakanomyo, Y. Shiokawa, A. A. Makanomyo, J. A. Mydosh, P. H. Kes, Ultrasonic attenuation in URu<sub>2</sub>Si<sub>2</sub>. *Jpn. J. Appl. Phys.* **26**, 1249 (1987).
37. G. Bullock, B. Shivaram, D. G. Hinks, Longitudinal ultrasound in the heavy electron superconductor URu<sub>2</sub>Si<sub>2</sub>. *Physica C Supercond.* **169**, 497–500 (1990).
38. B. Wolf, P. Thalmeier, G. Bruls, W. Sixl, D. Finsterbusch, B. Lüthi, Ultrasound propagation in the heavy-fermion superconductors URu<sub>2</sub>Si<sub>2</sub> and CeCu<sub>2</sub>Si<sub>2</sub>. *Physica B Conds. Matter.* **199**, 167–169 (1994).
39. T. Yanagisawa, H. Saito, Y. Watanabe, Y. Shimizu, H. Hidaka, H. Amitsuka, A study of elastic properties of URu<sub>2</sub>Si<sub>2</sub> in comparison with the non-*5f* contribution of ThRu<sub>2</sub>Si<sub>2</sub>. *J. Phys. Conf. Ser.* **391**, 012079 (2012).
40. T. Yanagisawa, S. Mombetsu, H. Hidaka, H. Amitsuka, P. T. Cong, S. Yasin, S. Zherlitsyn, J. Wosnitzer, K. Huang, N. Kanchanavatee, M. Janoschek, M. B. Maple, D. Aoki, Search for multipolar instability in URu<sub>2</sub>Si<sub>2</sub> studied by ultrasonic measurements under pulsed magnetic field. *Phys. Rev. B* **97**, 155137 (2018).
41. There are two A<sub>1g</sub> strains,  $\epsilon_{xx} + \epsilon_{yy}$  and  $\epsilon_{zz}$  with associated moduli  $(c_{11} + c_{12})/2$  and  $c_{33}$ , as well as linear coupling between these two strains that produces a third modulus  $c_{23}$ . To simplify the notation, we drop the sum over all three of these terms in the free energy.
42. K. A. Modic, M. D. Bachmann, B. J. Ramshaw, F. Arnold, K. R. Shirer, A. Estry, J. B. Betts, N. J. Ghimire, E. D. Bauer, M. Schmidt, M. Baenitz, E. Svanidze, R. D. McDonald, A. Shekhter, P. J. W. Moll, Resonant torsion magnetometry in anisotropic quantum materials. *Nat. Commun.* **9**, 3975 (2018).
43. R. Baumbach, Z. Fisk, F. Ronning, R. Movshovich, J. D. Thompson, E. D. Bauer, High purity specimens of URu<sub>2</sub>Si<sub>2</sub> produced by a molten metal flux technique. *Philos. Mag.* **94**, 3663–3671 (2014).
44. B. C. Száji, Approximation with Artificial Neural Networks, thesis, Faculty of Sciences, Eötvös Loránd University, Hungary (2001).
45. J. Buhot, M.-A. Méasson, Y. Gallais, M. Cazayous, A. Sacuto, G. Lapertot, D. Aoki, Symmetry of the excitations in the hidden order state of URu<sub>2</sub>Si<sub>2</sub>. *Phys. Rev. Lett.* **113**, 266405 (2014).
46. T. Ikeda, K. Fujibayashi, T. Nagai, J. Kobayashi, Elastic anomaly in (NH<sub>4</sub>)<sub>2</sub>SO<sub>4</sub>. *Phys. Stat. Solidi A* **16**, 279–290 (1973).
47. C. W. Garland, J. S. Jones, Elastic constants of ammonium chloride near the lambda point. *J. Chem. Phys.* **39**, 2874 (1963).
48. T. D. Matsuda, E. Hassinger, D. Aoki, V. Taufour, G. Knebel, N. Tateiwa, E. Yamamoto, Y. Haga, Y. Onuki, Z. Fisk, J. Flouquet, Details of sample dependence and transport properties of URu<sub>2</sub>Si<sub>2</sub>. *J. Phys. Soc. Japan* **80**, 114710 (2011).
49. A. Gallagher, W. L. Nelson, K. W. Chen, T. Besara, T. Siegrist, R. E. Baumbach, Single crystal growth of URu<sub>2</sub>Si<sub>2</sub> by the modified bridgman technique. *Crystals* **6**, 128 (2016).
50. N. Okuda, T. Suzuki, Z. Mao, Y. Maeno, T. Fujita, Unconventional strain dependence of superconductivity in spin-triplet superconductor Sr<sub>2</sub>RuO<sub>4</sub>. *J. Phys. Soc. Japan* **71**, 1134 (2002).
51. J. Greitemann, K. Liu, L. Pollet, Probing hidden spin order with interpretable machine learning. *Phys. Rev. B* **99**, 060404 (2019).
52. A. Migliori, J. D. Maynard, Implementation of a modern resonant ultrasound spectroscopy system for the measurement of the elastic moduli of small solid specimens. *Rev. Sci. Instrum.* **76**, 121301 (2005).
53. N. Harrison, M. Jaime, Hidden valence transition in URu<sub>2</sub>Si<sub>2</sub>? arXiv:1902.06588 [cond-mat.str-el] (18 February 2019).
54. P. Chandra, P. Coleman, R. Flint, Hysteric order in the heavy-fermion compound URu<sub>2</sub>Si<sub>2</sub>. *Nature* **493**, 621–626 (2013).
55. S. Altmann, P. Herzog, *Point-Group Theory Tables* (Clarendon Press, 1994).
56. W. Rehwald, The study of structural phase transitions by means of ultrasonic experiments. *Adv. Phys.* **22**, 721–755 (1973).
57. K. Miyake, C. M. Varma, Landau-Khalatnikov damping of ultrasound in heavy-fermion superconductors. *Phys. Rev. Lett.* **57**, 1627–1630 (1986).
58. K. Matsuda, Y. Kohori, T. Kohara, K. Kuwahara, H. Amitsuka, Spatially inhomogeneous development of antiferromagnetism in URu<sub>2</sub>Si<sub>2</sub>: Evidence from <sup>29</sup>Si NMR under pressure. *Phys. Rev. Lett.* **87**, 087203 (2001).
59. T. Yanagisawa, Ultrasonic study of the hidden order and heavy-fermion state in URu<sub>2</sub>Si<sub>2</sub> with hydrostatic pressure, Rh-doping, and high magnetic fields. *Philos. Mag.* **94**, 3775–3788 (2014).

**Acknowledgments:** We thank P. Coleman, P. Chandra, and R. Flint for the helpful discussions. **Funding:** Work at Los Alamos National Laboratory was performed under the auspices of the U.S. Department of Energy (DOE), Office of Basic Energy Sciences, Division of Materials Sciences and Engineering. M.M., B.J.R., and S.G. acknowledge support by the Cornell Center for Materials Research with funding from the NSF MRSEC program (DMR-1719875). M.M. acknowledges support by the NSF [Platform for the Accelerated Realization, Analysis, and Discovery of Interface Materials (PARADIM)] under cooperative agreement no. DMR-1539918. E.-A.K. acknowledges support from DOE DE-SC0018946. B.J.R. and S.G. acknowledge funding from the NSF under grant no. DMR-1752784. **Author contributions:** S.G. and B.J.R. designed the experiment. R.B. and E.D.B. grew sample S2. J.A.M. grew sample S1. S.G. acquired and analyzed the data. M.M. and E.-A.K. designed the ANN. K.A.M., A.S., M.M., S.G., and B.J.R. wrote the manuscript with input from all coauthors. **Competing interests:** The authors declare that they have no competing interests. **Data and materials availability:** All data needed to evaluate the conclusions in the paper are present in the paper and/or the Supplementary Materials. Additional data related to this paper may be requested from the authors.

Submitted 6 September 2019  
Accepted 10 December 2019  
Published 6 March 2020  
10.1126/sciadv.aaz4074

**Citation:** S. Ghosh, M. Matty, R. Baumbach, E. D. Bauer, K. A. Modic, A. Shekhter, J. A. Mydosh, E.-A. Kim, B. J. Ramshaw, One-component order parameter in URu<sub>2</sub>Si<sub>2</sub> uncovered by resonant ultrasound spectroscopy and machine learning. *Sci. Adv.* **6**, eaaz4074 (2020).

## One-component order parameter in URu<sub>2</sub>Si<sub>2</sub> uncovered by resonant ultrasound spectroscopy and machine learning

Sayak Ghosh, Michael Matty, Ryan Baumbach, Eric D. Bauer, K. A. Modic, Arkady Shekhter, J. A. Mydosh, Eun-Ah Kim and B. J. Ramshaw

*Sci Adv* **6** (10), eaaz4074.  
DOI: 10.1126/sciadv.aaz4074

### ARTICLE TOOLS

<http://advances.sciencemag.org/content/6/10/eaaz4074>

### SUPPLEMENTARY MATERIALS

<http://advances.sciencemag.org/content/suppl/2020/03/02/6.10.eaaz4074.DC1>

### REFERENCES

This article cites 53 articles, 3 of which you can access for free  
<http://advances.sciencemag.org/content/6/10/eaaz4074#BIBL>

### PERMISSIONS

<http://www.sciencemag.org/help/reprints-and-permissions>

Use of this article is subject to the [Terms of Service](#)

---

*Science Advances* (ISSN 2375-2548) is published by the American Association for the Advancement of Science, 1200 New York Avenue NW, Washington, DC 20005. The title *Science Advances* is a registered trademark of AAAS.

Copyright © 2020 The Authors, some rights reserved; exclusive licensee American Association for the Advancement of Science. No claim to original U.S. Government Works. Distributed under a Creative Commons Attribution NonCommercial License 4.0 (CC BY-NC).